Journal of Rock Mechanics and Geotechnical Engineering 18 (2026) 3949–3965

Contents lists available at ScienceDirect

Journal of Rock Mechanics and Geotechnical Engineering

journal homepage: www.jrmge.cn

Full Length Article

Seepage on 3D active earth pressure of unsaturated soils considering spatially variable hydraulic properties

Hui Chen [a,b], Qihao Jiang [a,b], Dongming Zhang [a,b,*], Yadong Xue [a,b], Hongwei Huang [a,b]

[a] Key Laboratory of Geotechnical and Underground Engineering of Ministry of Education, Tongji University, Shanghai, 200092, China
[b] Department of Geotechnical Engineering, Tongji University, Shanghai, 200092, China

ARTICLE INFO

Article history:
Received 28 December 2024
Received in revised form
29 March 2025
Accepted 29 June 2025
Available online 30 July 2025

Keywords:
Active earth pressure
Saturated hydraulic conductivity
Random field
Spatial variability
Retaining wall

ABSTRACT

Traditional active earth pressure evaluations considering seepage are typically deterministic, assuming uniform soil layers. However, soil hydraulic properties exhibit the obvious spatial variability due to geomorphological processes or poor construction control. To address this, the random limit analysis method (RLAM) is employed to investigate the influence of spatial variability of saturated hydraulic conductivity on active earth pressure. To combine random field simulations with the limit analysis-based evaluation method, this study discretizes the conventional three-dimensional (3D) rotational failure mechanism. Owing to the energy dissipation principle, the explicit expression of 3D active earth pressures can be derived. The proposed method's validity is demonstrated through comparisons with available analytical solutions, deterministic numerical calculations, and random finite difference method (RFDM). RLAM integrating with Monte Carlo simulations (MCS) in MATLAB, facilitates the probabilistic analysis of the active earth pressure to be evaluated. The findings indicate that the present method not only incorporates the spatial variability of hydraulic properties, but also enhances the computational efficiency of calculating active earth pressures compared to the RFDM. Based on extensive uncertainty analyses, this study proposes a system reliability evaluation method for semi-gravity retaining walls, accounting for the spatial variability of saturated hydraulic conductivity. The results reveal that under different random field design scenarios, all decay curves of system failure probabilities for a semi-gravity retaining wall intersect within a specific range, referred to herein as the "turning region". Furthermore, as the normalized horizontal autocorrelation distance, anisotropic ratio and coefficient of variation increase, the effective influence zone of the wall design index on system failure probability gradually expands, offering valuable guidance for the design and construction of semi-gravity retaining walls.

1. Introduction

A retaining wall is typically constructed to support embankments or soil slopes, preventing the soil displacement, and potential instability. Determining active earth pressure is crucial for evaluating the wall's stability against sliding and overturning (Vahedifard et al., 2015). Over the years, various studies have primarily focused on enhancing computational models to rapidly provide deterministic predictions of three-dimensional (3D) active earth pressure (Piaskowski and Kowalewski, 1965; Huder, 1972; Soubra et al., 2000; Yang and Li, 2018; Li et al., 2021). In the present study, the concept of "equivalent width" for irregular failure surfaces proposed by Yang and Li (2018) has been adopted. This definition addresses scenarios where 3D failure mechanism does not fully cover the entire soil-wall interface, thereby enabling a more accurate evaluation of 3D active earth pressure. Moreover, in practical engineering, the backfill behind retaining walls is affected by various factors, such as rainfall infiltration and moisture evaporation. This causes water to migrate through the soil, a process called seepage, which shifts the distribution of soil effective stress and ultimately affects the active earth pressure (Li, 2023).

* Corresponding author. Key Laboratory of Geotechnical and Underground Engineering of Ministry of Education, Tongji University, Shanghai, 200092, China.
E-mail address: 09zhang@tongji.edu.cn (D. Zhang).

Peer review under responsibility of Institute of Rock and Soil Mechanics, Chinese Academy of Sciences.

https://doi.org/10.1016/j.jrmge.2025.06.015

Bishop (1959) first introduced a concept to characterize the stress state above the groundwater table, emphasizing the role of negative porewater pressure or matric suction in defining the shear strength of unsaturated soils. Lu and Likos (2004) introduced the suction stress characteristic curve (SSCC), a constitutive model that redefines matric suction not as an independent stress variable but as a hysteretic state variable governed by physicochemical soil-water interactions. Their theory decouples suction stress from effective stress, explicitly capturing path-dependent hysteresis observed in clays, as validated through experimental researches in Lu and Likos (2006). Lu et al. (2010) formulated an equation linking effective stress to matric suction within the framework of classical thermodynamics. This equation depends on two controlling parameters: the air-entry value and the pore size distribution index. Recent studies have increasingly used state variables to assess the impact of suction stress on slope stability and geotechnical structures (e.g. Vahedifard et al., 2015; Cheng et al., 2022). However, the abovementioned methods for seepage analysis are deterministic, treating soil properties as constant within a given layer and assuming homogeneity (Gui et al., 2000), and the accuracy depends heavily on precise input parameter determination. However, the aforementioned studies have seldom focused on probabilistic analysis, with their accuracy heavily relying on the precise determination of input parameters. In practical applications, input parameters exhibit uncertainties arising from inherent soil variability, measurement errors, model uncertainties, and other factors. To better understand these uncertainties, it is essential to analyze problems from a stochastic perspective (Tsompanakis et al., 2009; Li et al., 2021).

Methods such as Monte Carlo simulation (MCS), first-order reliability method (FORM), or response surface method (RSM) have accordingly been developed for probabilistic evaluation of geotechnical problems (Castillo et al., 2004; Zevgolis and Bourdeau, 2010; Gao et al., 2019). Li et al. (2021) performed a probabilistic analysis of active earth pressures utilizing the sparse polynomial chaos expansion (SPCE) and proposed a reliability evaluation method for retaining walls incorporating multiple random variables. However, these stochastic methods are often restricted to homogeneous mediums, failing to account for the spatial correlation and continuity of soil properties. To overcome the limitation, the random field theory was widely employed to model the spatial variability of soil properties (Griffiths and Fenton, 2004; Liu et al., 2017; Pieczyńska-Kozłowska and Vessia, 2022; Zhang et al., 2024). Available researches suggest that random fields provide a more accurate representation of soil behaviors compared to using representative values or simple random variables (Johari et al., 2020; Zhang et al., 2021; Ng et al., 2022; Shi and Wang, 2023; Chen et al., 2024). Specifically, the combination of random field simulations with numerical methods, such as the random finite difference method (RFDM), has become a preferred approach for addressing spatial variability in soil parameters. Nevertheless, it encounters challenges in 3D geotechnical cases due to substantial computational costs. For this, Cheng et al. (2019) introduced an effective technique known as the random limit analysis method (RLAM), which combines random field simulations with a kinematic approach to capture the optimal failure surface of the tunnel face. More recently, Li et al. (2024) extended a semi-analytical method to assess the probabilistic stability of slopes with uncertain shear strengths. To the authors' knowledge, scarce research has yet applied this approach to evaluation of 3D active earth pressure.

This study mainly aims at quantifying the influence of seepage that considers 3D spatial variability of hydraulic properties on active earth pressures. To combine the limit analysis with stochastic method to characterize the spatial variability of hydraulic parameters, the conventional 3D failure model is specially discretized. The proposed method's validity is demonstrated through comparisons with results from the upper-bound finite element method and numerical simulations under the same conditions. Results show that RLAM can effectively account for the spatial variability of hydraulic properties, requiring a lower computational cost compared with the RFDM. Additionally, based on extensive uncertainty computation results, this study improves a system reliability evaluation method for retaining walls that accounts for the spatial variability of saturated hydraulic conductivity, providing valuable guidance for the design and construction of semi-gravity retaining walls.

2. Steady seepage analysis

Negative pore water pressure exists in the unsaturated zone of the soil, also known as the matric suction, which can increase effective stress and enhance shear strength. Moreover, matric suction alters the movement of moisture within the soil, affecting its permeability and water retention capacity. Extensive experimental data on unsaturated soils reveal a notable nonlinear relationship between the soil strength and the suction stress (Vanapalli et al., 1996). Bishop (1959) extended the classical effective stress principle using the concepts of pore-air pressure u_a and negative pore water ($u_a - u_w$), with the expression written as

$$\sigma' = (\sigma - u_a) + \chi(u_a - u_w) \tag{1}$$

where σ is equal to the total stress; σ' is equal to the effective stress; u_w denotes pore-water pressure; χ is a dimensionless coefficient, representing soil's saturation degree. According to Bishop's definition, $\chi = 0$ means that the soil is fully dry, while $\chi = 1$ means that the soil is fully saturated.

While Bishop's effective stress theory provides a foundational framework for unsaturated soils, its direct application to clayey soils faces challenges due to the significant contribution of van der Waals attraction to suction stress, which is not explicitly captured by the χ parameter. Therefore, Lu and Likos (2004) proposed the concept of suction stress to explain the changes in effective stress driven by matric suction:

$$\sigma' = \sigma - u_a - \sigma^s \tag{2}$$

where σ^s represents suction stress.

Notably, in granular soils where hysteresis arises primarily from capillary effects, Bishop's theory can approximate hysteretic behavior if coupled with a hysteretic soil-water retention curve (SWRC) model. Lu et al. (2010) proposed a closed-form expression for σ^s, which is solely dependent on matric suction and derived within the framework of thermodynamics:

$$\sigma^s = \begin{cases} -(u_a - u_w) & (u_a - u_w \le 0) \\ -\dfrac{u_a - u_w}{\left\{1 + [\alpha(u_a - u_w)]^n\right\}^{\frac{n-1}{n}}} & (u_a - u_w > 0) \end{cases} \tag{3}$$

The inverse of the air-entry value, α and pore size distribution, n, together describe the soil's water absorption capacity and its pore structure (Vahedifard et al., 2015). Fig. 1 gives the distribution of α and n for diverse soil types. It is evident that the air entry value is highest for clay, followed by silt, and lowest for sand, while the pore size distribution shows the opposite trend for these three soil types. The first item of Eq. (3) describes the suction stress existing in saturated soils, aligning with the classical effective principle ($\sigma' = \sigma - u_w$). In contrast, the second item of Eq. (3) applies to unsaturated soil conditions and addresses the limitations of

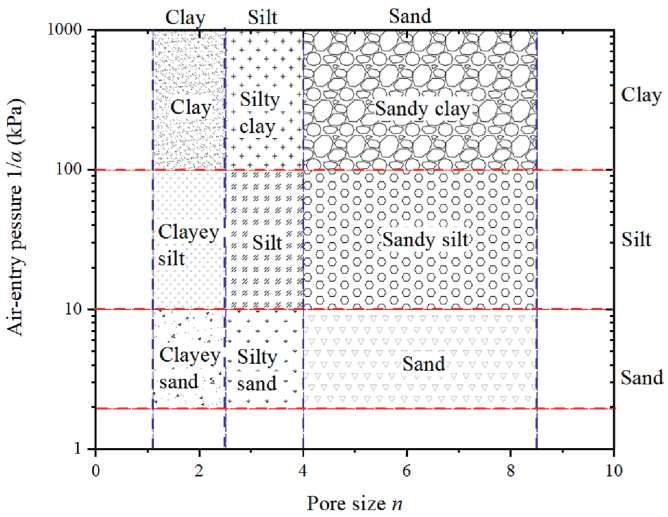

Fig. 1. Range of representative α and n of different soils (Vahedifard et al., 2015).

Bishop's method by incorporating non-zero suction stress in dry soils. The Gardner's (1958) model describes the soil water retention curve, revealing the relationship between matric suction and soil water content. Combined with Darcy's law, the distribution of matric suction as a function of depth can be derived:

$$u_a - u_w = -\frac{1}{\alpha}\ln\left[\left(1+\frac{q}{k_s}\right)e^{-\gamma_w \alpha z} - \frac{q}{k_s}\right] \tag{4}$$

where q refers to the flow velocity (with $q > 0$ for evaporation, $q < 0$ for infiltration, and $q = 0$ for hydrostatic condition). k_s refers to the saturated hydraulic conductivity. z refers to the vertical distance from the waterline to any point. γ_w refers to the unit weight of water.

Note that the value inside the logarithm of Eq. (4) must be greater than 0. Additionally, this value should be no more than 1.0, in order to ensure non-negative matric suction. Such constraint is crucial for accurately determining unsaturated shear strength and for subsequent calculations that account for the spatial variability of saturated hydraulic conductivity. Notably, under hydrostatic conditions ($q = 0$), matric suction follows a linear distribution along the vertical direction:

$$u_a - u_w = z\gamma_w \tag{5}$$

By integrating Eqs. (3) and (4), the expression of suction stress can be derived as

$$\sigma^s = \frac{1}{\alpha}\frac{\ln\left[\left(1+\frac{q}{k_s}\right)e^{-\gamma_w \alpha z} - \frac{q}{k_s}\right]}{\left\{1+\left\{-\ln\left[\left(1+\frac{q}{k_s}\right)e^{-\gamma_w \alpha z} - \frac{q}{k_s}\right]\right\}^n\right\}^{(n-1)/n}} \tag{6}$$

Suction stress is a product influenced by various factors, including complex hydraulic characteristics and different flow boundary conditions. These factors can improve the unsaturated shear strength. Within the unified effective stress framework, the modified Mohr–Coulomb (MC) failure criterion is employed to characterize the soil shear strength:

$$\tau = c' + (\sigma - u_a)\tan\varphi' - \sigma^s \tan\varphi' \tag{7}$$

where τ represents the soil shear strength, and φ' denotes the effective internal friction angle.

The parameter c_{app} is defined as an apparent cohesion that is governed by σ^s and φ', and can be written by

$$c_{app} = -\sigma^s \tan\varphi' = f(k_s, q, \alpha, n, z, \varphi') \tag{8}$$

where c_{app} can be regarded as a function associated with soil and hydraulic parameters. Table 1 presents the soil and hydraulic parameters of four hypothetical soils: clay, silt, loess, and sand, along with three flow velocities corresponding to high infiltration, no flow, and high evaporation.

Fig. 2 illustrates the normalized suction stress profiles for four hypothetical soils under varying flow velocities q and wall heights H. In this study, the water level is assumed to be a constant at the base of the retaining wall, ensuring that soils remain unsaturated. Previous studies have demonstrated that rising water levels can significantly increase active earth pressure, and matric suction vanishes when soil masses are absolutely submerged (Yang and Chen, 2021). However, the present study mainly focuses on analyzing how spatial variability in saturated hydraulic conductivity influences 3D active earth pressure, and thus the effect of water levels is not discussed herein. It should be noted that suction stress is negative because in soil mechanics, the compressive stress is defined as the positive. Overall, the higher the retaining wall, the lower the suction stress corresponding to the normalized vertical distance, which applies to all hypothetical soils. Different soils exhibit significant variations in response to flow velocities within a given location. For clay, suction stress is the lowest under infiltration conditions, the higher under no-flow conditions, and the highest during evaporation. The further the suction stress is from the water table, the greater its value. Additionally, the effect of flow velocities on suction stress is much greater than that of retaining wall height. Silt and loess present similar behavior, with variations in flow velocities having minimal influence on suction stress. Moreover, the relationship between suction stress and normalized vertical distance is no longer monotonic. At a wall height of 1m, suction stress increases approximately linearly with normalized vertical distance z/H. As H grows, suction stress initially increases and then decreases, with this trend being more pronounced in loess. For sand, the suction stress shows a clear pattern of initially increasing, then decreasing, and finally approaching zero. As wall height $H = 1$ m, the maximum suction stress occurs at a normalized vertical distance of 0.125. For heights of 4 m and 7 m, the corresponding distances are 0.2 and 0.8, respectively. It is worth mentioning that these soil types differ by an order of magnitude, and their corresponding saturated hydraulic conductivities are also distinct. Statistically, this differentiation does not conflict with the random field simulation that accounts for the spatial variability of soil parameters (Cho, 2012; Ng et al., 2024).

3. Material and methods

3.1. Discretized failure mechanism of supported soil masses

Previous studies suggest that a vertical slope behind the retaining wall may be prone to toe failure, with the failure surface typically extending through the slope toe (Pan et al., 2017; Li, 2023). It is well acknowledged that the upper-bound theorem requires the failure model to satisfy kinematic permission conditions. Michalowski and Drescher (2009) introduced a 3D rotational collapse block, aiming at evaluating the stability of slopes. Such predefined geometric mechanism is quite suitable for characterizing homogeneous layers. Nevertheless, it becomes less effective when soil parameters change irregularly with their spatial location. The failure mechanism adopted in this study is hence constructed by spatially discretizing points according to specific rules,

Table 1
Typical values of hydraulic parameters and flow velocities for four hypothetical soils.

Soil types	n	α (kPa^{-1})	k_s (m/s)	c' (kPa)	φ'(°)	Infiltration velocity (m/s)	No flow (m/s)	Evaporation velocity (m/s)
Clay	2	0.005	5×10^{-8}	5	20	-3.14×10^{-8}	0	1.15×10^{-8}
Silt	3	0.01	1×10^{-7}	3	25	-3.14×10^{-8}	0	1.15×10^{-8}
Loess	4	0.025	1×10^{-6}	1	28	-3.14×10^{-8}	0	1.15×10^{-8}
Sand	5	0.1	3×10^{-5}	0	30	-3.14×10^{-8}	0	1.15×10^{-8}

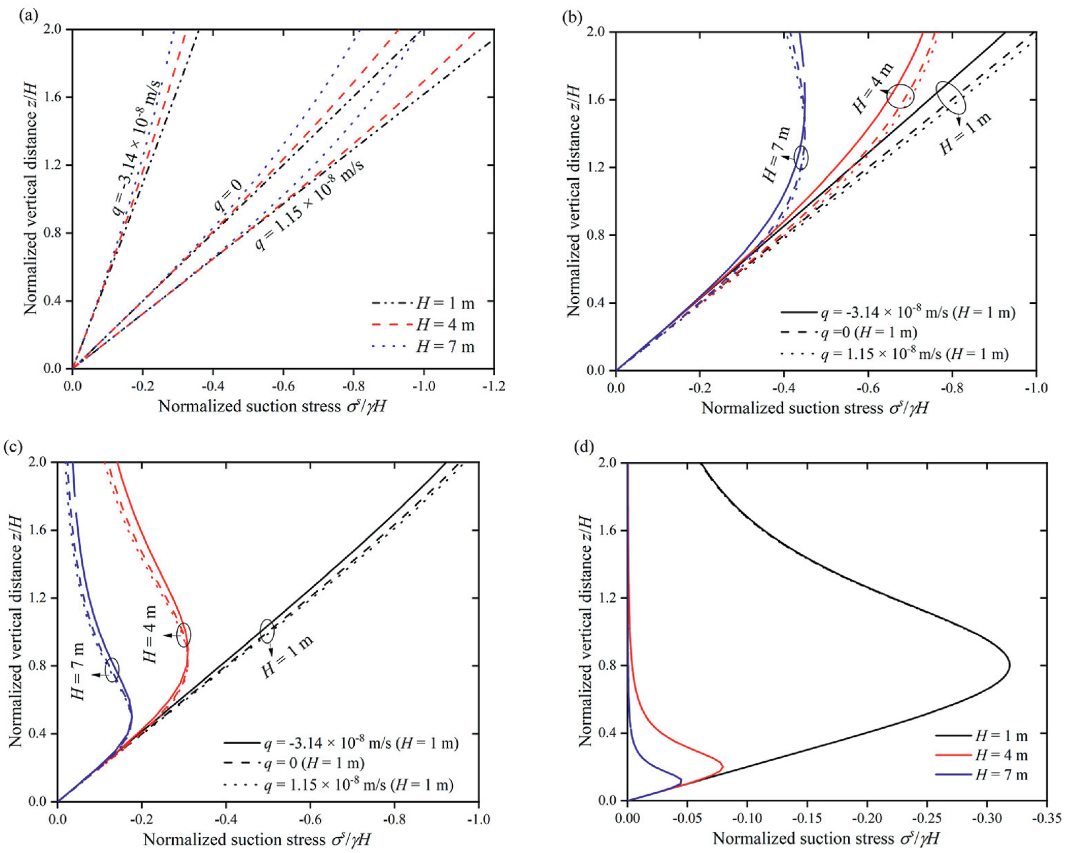

Fig. 2. Normalized suction stress profiles for different flow velocities and wall heights: (a) Clay, (b) silt, (c) loess, and (d) sand.

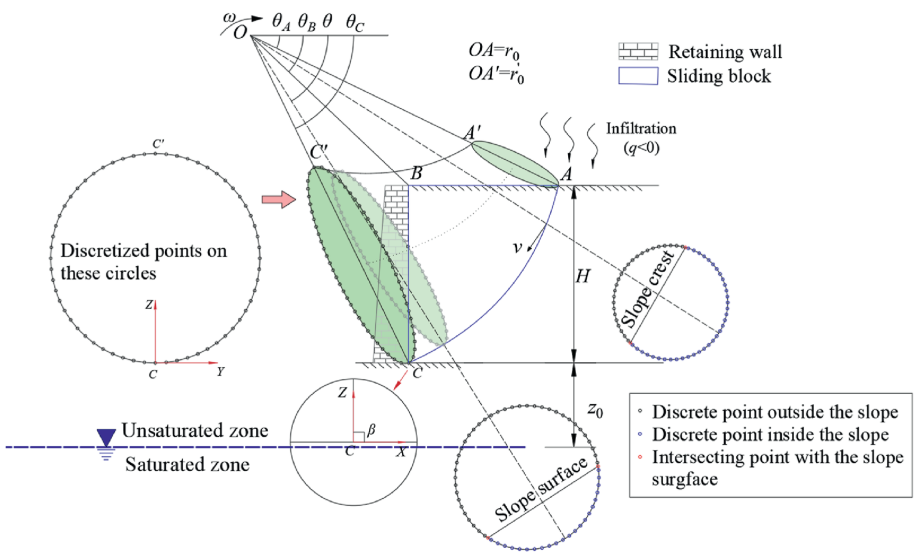

Fig. 3. Schematic diagram for 3D failure mechanism of the backfill behind the wall.

as described in Fig. 3, encompassing both the interior and exterior of a slope with the inclined angle β. Initially, it is divided into multiple planes centered around the rotation point O, aligned with the longitudinal direction of the backfill and confined between the angles θ_A and θ_C. A coordinate system X-Y-Z is constructed with its origin at the slope toe C. To guarantee the generation of discrete failure mechanism, the first circle is defined on the plane OA, with evenly distributed points along its diameter, which coincides with AA'. The hypothetical boundary condition aligns with the work of Michalowski and Drescher (2009), and the discretization technique allows to generate a complete failure mechanism, starting from the initial circle AA' and progressing to the final circle CC'. Two log-spirals AC and $A'C'$ define the boundaries of the curved cone, which can be expressed as

$$r_{AC}(\theta) = r_0 \exp[(\theta - \theta_0)\tan\varphi'] \tag{9}$$

$$r_{A'C'}(\theta) = r'_0 \exp[-(\theta - \theta_0)\tan\varphi'] \tag{10}$$

where r_0 and r'_0 are the initial distances between the rotation center O and two initial points, respectively; and θ_0 is the initial polar angle between the X-axis and the line OA. As depicted in Fig. 3, the slope surface, BC, is perpendicular to the horizontal surface AB. The geometrical relationship of angles θ_A, θ_B and θ_C can be derived as

$$\theta_B = \arccos\frac{\cos\theta_0 - L/r_0}{\sqrt{(\cos\theta_0 - L/r_0)^2 + \sin^2\theta_0}} \tag{11}$$

where L represents the length between A and B, which can be written as

$$L/r_0 = \left[\sin(\theta_0+\beta) - \sin(\theta_C+\beta)e^{(\theta_C-\theta_0)\tan\varphi'}\right]/\sin\beta \tag{12}$$

As shown in Fig. 4, the crucial step that constructs a discrete failure mechanism involves generating a new point on the subsequent plane Π_{j+1} using any neighboring points from the preceding plane Π_j. Given the known points $P_{i,j}$ and $P_{i+1,j}$, the coordinates of the new point $P_{i,\,j+1}$ can be determined by solving the corresponding equation:

$$\begin{cases} \vec{v}_j \cdot \vec{N} = \cos(\pi/2 + \varphi') \\ \theta_{j+1} = \arctan\left(\dfrac{YO - YP_{i,j+1}}{ZO - ZP_{i,j+1}}\right) \\ \alpha_{i,j+1} = \dfrac{\alpha_{i,j} + \alpha_{i+1,j}}{2} \end{cases} \tag{13}$$

where $\vec{v}_j$ is the unit velocity vector of the plane Π_j; $\vec{N}$ is normal vector of the plane enclosed by points $P_{i,j}$, $P_{i+1,j}$ and $P_{i,j+1}$; $\theta_{i,j+1}$ is the rotation angle of the subsequent plane Π_{j+1}; $YP_{i,j+1}$, $ZP_{i,j+1}$ are Y-coordinate and Z-coordinate of the point $P_{i,j+1}$, respectively; YO and ZO are Y-coordinate and Z-coordinate of the rotation center O, respectively; $\alpha_{i,j}$ represent the angle at which a discrete point $P_{i,j}$ deviates from the circle center C_j in the local coordinate system Y-C_j-Z'. Similarly, angles $\alpha_{i+1,j}$, $\alpha_{i,j+1}$ and $\alpha_{i+1,j+1}$can be readily defined. The accuracy of this failure mechanism depends on two discretization parameters: N_{um}, which represents the number of radial circles, and δ_θ, which indicates the angle between adjacent radial planes. It is worth noting that the location of the subsequent point $P_{i,j+1}$ on the mid-perpendicular line of the line AB. In Eq. (13), the first equation ensures compliance with the associated flow rule during the generation of the mechanism. The second equation ensures that newly generated points lie in the same plane. The third equation ensures the uniform distribution of points on the subsequent plane. Once the two known points on the previous plane are given, Eq. (13) uniquely determines the new point.

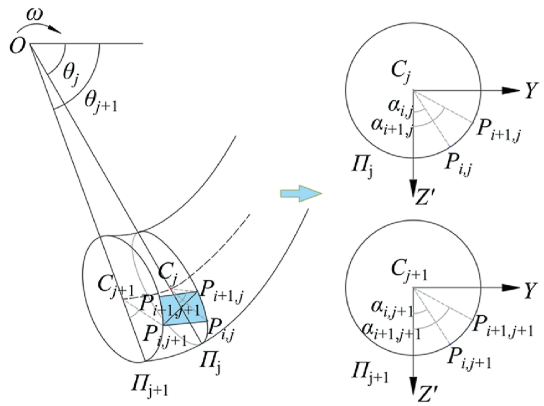

Fig. 4. The principle of generating new points using the spatial discretization technique.

Furthermore, to account for the impact of slope width on soil stability, a plane strain insert is accordingly introduced into the discrete failure mechanism, as shown in Fig. 5. This insert is formed by dividing the two halves of the 3D failure surface. Spatial discretization is then applied to generate the plane insert region, with its lower boundary defined by a log spiral at the slope toe. The insert's boundaries smoothly align with the failure mechanism's symmetry plane. In this scenario, the width of the insert block can be determined by

$$b_W = B_W - B_{max} \tag{14}$$

where B_W and B_{max} represents the total width of the backfill and the maximum width of 3D rotational collapse mechanism. Such width of the inserted block, b_W, is a variable to be optimized, which significantly contributes to the objective function.

3.2. Characterization of saturated hydraulic conductivity using random fields

Traditional seepage analysis usually assumes hydraulic properties to be constant, treating soil layer as homogeneous. Generally, this assumption can satisfy applications of engineering designers. However, hydraulic properties of soils exhibit notable spatial variations across different layers due to stratification (Srivastava et al., 2010; Huo et al., 2023; Ng et al., 2024), with fluctuations at a finer scale within each individual layer. Consequently, such homogeneous assumption may cause suboptimal results (Liu et al., 2016). In this context, random field simulation proves effective for characterizing the soil permeability based on limited stratigraphic data. The autocorrelation distance, or scale of fluctuation, plays a crucial role in this process. This correlation gradually weakens as the distance between the points increases. Specifically, the hydraulic property is modeled as a spatial random field following a normal distribution, with consideration for heterogeneity by allowing a larger scale of fluctuation in the horizontal direction compared to the vertical direction (Cho, 2012; Li et al., 2024). The autocorrelation distance along the horizontal direction (l_x,l_y) is herein define as ξ, and the anisotropy ratio k is used to describe the anisotropic characteristics of the random field. Accordingly, the vertical autocorrelation distance l_z is equal to $k\xi$ ($0 < k \leq 1$). If the anisotropy ratio is close to 1, it indicates that the autocorrelation is relatively uniform in all directions, and the

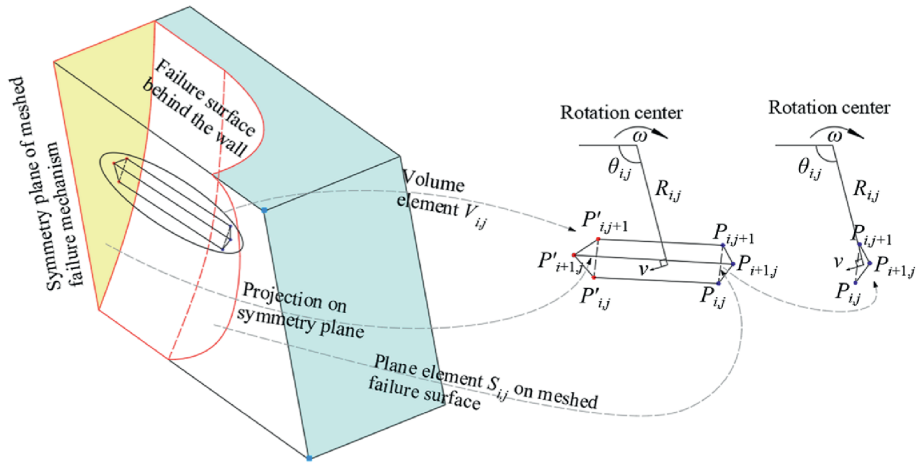

Fig. 5. Schematic diagram of discrete failure mechanism with the discrete plane insert.

random field is nearly isotropic. If the anisotropy ratio is much less than 1, it indicates that the range of correlation in the vertical direction is significantly smaller than in the horizontal direction, and the random field exhibits pronounced anisotropy. Furthermore, saturated hydraulic conductivity k_s controls steady seepage field and matric suction, which is pivotal in the shear strength of unsaturated soils (Ng and Shi, 1998; Santoso et al., 2011; Masoudian et al., 2019). Variations in k_s can lead to changes in unsaturated shear strength, directly impacting the structural integrity of retaining walls. Therefore, the 3D Gaussian autocorrelation function can be expressed as

$$\rho_s = \exp\left[-2\left(\frac{|\Delta_x|}{\xi}+\frac{|\Delta_y|}{\xi}+\frac{|\Delta_z|}{k\xi}\right)\right] \tag{15}$$

where Δ_x, Δ_y and Δ_z are referred to spatial coordinate disparities between any two points.

To optimize the application of stochastic finite difference models, discretization of the stochastic field is essential. The Karhunen-Loève (K-L) expansion method, distinguished by its superior computational efficiency and precision, excels in random field discretization compared to alternative techniques (Cheng et al., 2019; Tan et al., 2020). It transforms the stratigraphic coordinates into independent random variables with high accuracy. To avoid the occurrence of negative values of hydraulic parameters, a lognormal random field for the saturated hydraulic conductivity k_s can be derived:

$$R_{k_s}(x,y,z) = \exp\left[\lambda_{\ln k_s} + \zeta_{\ln k_s} N(x,y,z)\right] \tag{16}$$

where (x, y, z) denotes the spatial location of any point, N denotes a standard normal random field. Then, the mean $\lambda_{\ln k_s}$ and the standard deviation $\varsigma_{\ln k_s}$ of the logarithmic saturated hydraulic conductivity $\ln k_s$ are obtained by

$$\lambda_{\ln k_s} = \ln \mu_{k_s} - \frac{1}{2}\zeta^2_{\ln k_s} \tag{17}$$

$$\varsigma_{\ln k_s} = \sqrt{\ln\left(1+COV^2_{k_s}\right)} \tag{18}$$

where μ_{k_s}, COV_{k_s} refer to the mean value and coefficient of variation of saturated hydraulic conductivity k_s. Fig. 6a depicts a random field realization R_{k_s} for a vertical slope with slope height $H = 5$m and a width-to-height ratio $B/H = 2$. The random fields are created using the fast Fourier transform-moving average method, incorporating the saturated hydraulic conductivity statistics as: $\mu_{k_s} = 5 \times 10^{-8}$ m/s, $COV_{k_s} = 0.3$. At this case, the normalized autocorrection distance $\xi/H = 0.5$, and 2.5 corresponding anisotropy ratio remains constant $k = 0.2$. Based on these random field parameters, Fig. 6a describes the possible spatial distribution of saturated hydraulic conductivity in a 3D formation. As elaborated in Section 2, the functional relationship between the apparent cohesion of unsaturated soil and hydraulic parameters has been derived, thereby enabling the determination of the potential spatial distribution of apparent cohesion. It should be noted that, due to the inherent variability of saturated hydraulic conductivity, the derived apparent cohesion may assume negative values in certain regions, as illustrated in Fig. 6b. Since negative cohesion values are not physically plausible, these areas are adjusted to zero to ensure the accuracy.

To intuitively illustrate the impact of spatial variability of hydraulic properties on the soil stability, Fig. 7 shows the distribution of the saturated hydraulic conductivity k_s along a potential sliding surface. The random field realizations of apparent cohesion corresponding to the potential failure surfaces are presented under both scenarios: with and without plane strain insert consideration. Compared to the uniform increase of apparent cohesion with height in a homogeneous clay model, the distribution along the potential sliding surface is irregular and fragmented into discrete blocks. It should be clarified that although the sliding surface is kinematically admissible, it is not the optimal one. To address this, the next section will introduce an optimization program designed to identify the maximum active earth pressure and the most dangerous sliding surface.

3.3. Active earth pressure determinations

After defining the geometry feature of the failure surface, the analytical solution for active earth pressures is derived by formulating and solving the work rate balance equation as follows:

$$W_\gamma + W_{P_a} = D_{c'} + D_{c_{app}} \tag{19}$$

As illustrated in Fig. 3, the area enclosed by the blue line is the sliding block. In Eq. (19), the external work rates, W_γ and W_{P_a}, are produced by the soil weight γ of the sliding block and the reactive force of active earth pressure P_a, respectively. The dissipated energy consists of two components, $D_{c'}$ and Dc_{app}, which are caused by soil's effective cohesion c' and apparent cohesion c_{app}. The total work rate exerted by a force can be calculated by summing the

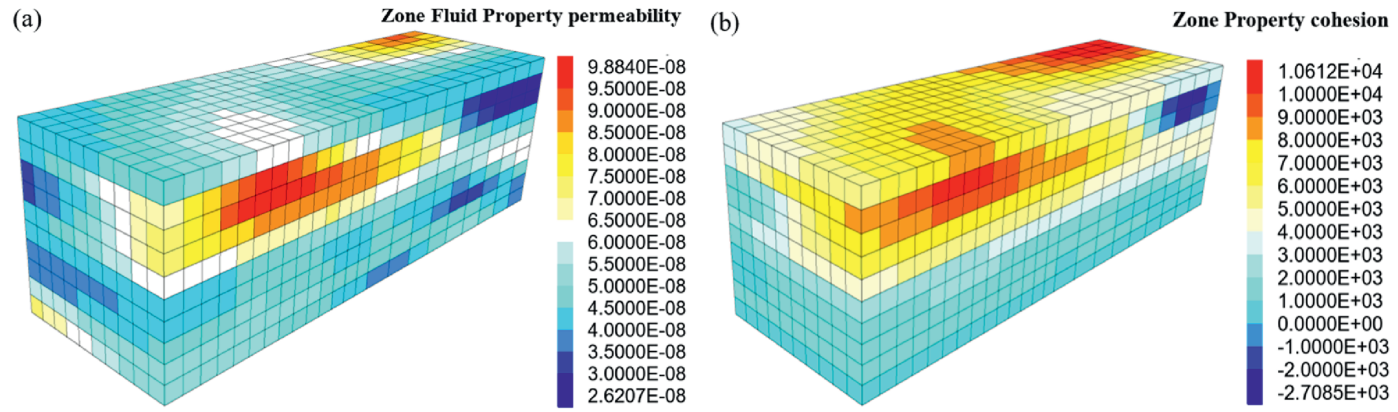

Fig. 6. Generation of spatial random fields: (a) possible spatial distribution of saturated hydraulic conductivity k_s, and (b) corresponding spatial distribution of apparent cohesion c_{app}.

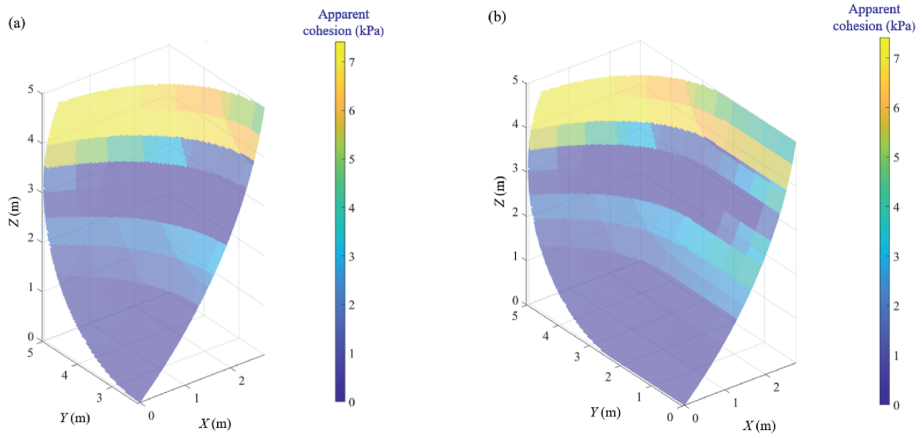

Fig. 7. Random field realizations of apparent cohesion assigned to 3D rotational collapse surface: (a) without plane insert, and (b) with plane insert.

work rates across all computational elements, which are defined by the discretized points of the failure mechanism. As depicted in Figs. 4 and 5, three adjacent points on planes Π_j and Π_{j+1} form a triangle, ensuring full coverage of the failure surface without overlap. Work rate calculations differ for volume forces and surface forces. By integrating these elements, the work rate done by soil weight is derived by

$$W_\gamma = \omega\gamma \sum_{i,j} \left(R_{i,j} V_{i,j} \cos\theta_{i,j} \right) \tag{20}$$

where γ refers to unit soil weight, $\theta_{i,j}$ refers to the polar angle corresponding to the rotation radius $R_{i,j}$, and $V_{i,j}$ refers to the elementary volume. j denotes the number of planes of discrete failure mechanism, and i denotes the number of evenly distributed points on each plane's circle. Similarly, the internal energy dissipation $D_{c'}$ and Dc_{app} are expressed as

$$D_{c'} = \omega c' \cos\varphi' \sum_{i,j} \left(R_{i,j} S_{i,j} \right) \tag{21}$$

$$D_{c_{app}} = \omega c_{app} \cos\varphi' \sum_{i,j} \left(R_{i,j} S_{i,j} \right) \tag{22}$$

where $S_{i,j}$ represents the elementary failure surface, and $R_{i,j}$ represents the rotation radius from rotation center to elementary failure surface.

The geometry relationships of the velocity vector, surface element and volume element are illustrated in Fig. 5. The supporting force of a retaining wall equals the resultant of active earth pressures, but in the opposite direction. Considering the difficulty in determining the precise distribution of active earth pressure in 3D scenarios, it is common that the action point of the resultant earth pressure is located at one-third of the wall height from the base. This simplification is particularly prevalent in earth pressure calculations (Qin and Chian, 2020). The specific expression of work rate done by the supporting force is written as

$$W_{P_a} = -\omega\sigma_c \sum_j \left[A_j \cos\left(\beta + \theta_j\right) \right] \tag{23}$$

where σ_c is the unit earth pressure along the wall height, and A_j is the unit area that the jth plane of the discrete failure mechanism covered on the retaining wall. θ_j is the rotation angle corresponding to the jth plane. More details can refer to as Li (2023)' work. The negative sign herein means the earth pressure does the negative work. Incorporating Eqs. (20)–(23) into Eq. (19), and the resultant active earth pressure is

$$P_a = \frac{W_\gamma - D_{c'} - D_{c_{app}}}{W_{P_a}/P_a} \tag{24}$$

To facilitate the optimization of retaining wall design, a dimensionless function is commonly employed to characterize the

interaction between soils and structures, written as the following form:

$$K_a = \frac{2P_a}{\gamma H^2 B_e} \tag{25}$$

where K_a refers to active earth pressure coefficient, and B_e is the equivalent width. As observed in Fig. 5, the sliding block does not span the whole interface, implying that parts of the wall are not subjective to earth pressures. Thus, the equivalent width is determined by the width of a rectangle whose area matches the area of the wall back affected by the sliding block. According to such description, the equivalent width can be calculated by

$$B_e = \frac{A}{H/\sin\beta} \tag{26}$$

where A is the area covered by the sliding block, which can be found in Yang and Li (2018).

As elaborated earlier, the kinematic limit analysis approach provides a closed solution for active earth pressures. Therefore, the optimal solution is identified as the maximum value among all possible outcomes that most closely approximates the actual solution. To identify this, a maximization scheme, namely sequential quadratic programming (SQP) in MATLAB is employed. Furthermore, the objective function is constrained by three independent variables: θ_A, θ_C and r_0/r'_0. Initially, an exhaustive method-based algorithm identifies a feasible starting point based on these constraints. Sequential quadratic programming then refines this to deliver a globally optimal solution. Thus, evaluating active earth pressures can be mapped as a mathematical optimization problem with the analytical form written as

$$K_a = \max : f\left(\theta_A, \theta_C, r'_0/r_0 \middle| c', \varphi', \gamma, \beta, H, B_W / H, q, k_s, \alpha, n\right) \tag{27}$$

It considers soil properties (c', φ', γ), geometry parameters (β, H, B_W/H), and hydraulic properties (q, k_s, α, n). The objective function should be solved under the following constraints:

$$\begin{cases} 0 < \theta_A < \theta_B < \theta_C < \pi \\ 0 < r'_0/r_0 < 1 \\ 0 < b_W < B_W \end{cases} \tag{28}$$

Additionally, Fig. 8 presents a flowchart that details the random field implementation and active earth pressure derivation. In the first stage, a representative soil type and its model size are selected, and the region is discretized into 0.5 m cubes. Random field simulations are then employed to generate the spatial distribution of apparent cohesion relevant to saturated hydraulic conductivity. In the second stage, active earth pressures are derived through establishing a work rate balance equation that incorporates the spatial variability of apparent cohesion along the failure surfaces. Finally, a nonlinear optimization technique is applied to calculate 3D active earth pressures.

4. Validation of RLAM

4.1. Compared to the finite element-based upper-bound limit analysis

The analytical solution in the present study involves a kinematic framework for evaluating 3D active earth pressure. Therefore, to validate the proposed approach, it is essential to comparatively illustrate results of several representative cases in conjunction with existing research. Antão et al. (2016) employed limit analysis to carry out numerical simulations, leveraging highly refined finite element meshes to model the complex 3D interaction between soil and retaining walls. That is a specific deterministic scenario considered in this study, specifically under the condition of $\beta = 90°$, $c' = 0$. Note that in this section, the wall back is assumed to be perfectly smooth, meaning the external friction angle is set to 0. Table 2 compares the active earth pressure coefficients from Antão et al. (2016) with those obtained in this study. The relative error is under 5 %, demonstrating that the present method accurately evaluates active earth pressures. Additionally, this study integrates the spatial variability of permeability in seepage into the kinematic framework, thereby advancing the existing analytical methods.

4.2. Deterministic numerical validation

A deterministic numerical model of 3D retaining wall is simulated by FLAC3D software, as illustrated in Fig. 9, aiming at performing a numerical validation. Due to the symmetry of the subject under study, it is sufficient to model only one half of the object. To mitigate boundary effects, a surrounding rock layer is added around the soil-wall system, smoothly connected to it. Normal constraints are applied around the entire model with model bottom fully fixed. Both the width and height of the wall are taken as 5m. To simulate the interaction between soil masses and walls, interface elements are herein employed. The normal stiffness is $K_n = 1.4 \times 10^9$ Pa/m, while the shear stiffness is $K_s = 1.4 \times 10^9$ Pa/m. Here, only the scenario where the back of the retaining wall is smooth is considered. The soil parameters behind the wall are taken as: unit soil weight $\gamma = 20$ kN/m^3, elastic module $E = 27$ MPa, Poisson's ratio $\upsilon = 0.35$, modeled by the MC failure criterion. The material parameters for adjacent rock layers or structures can be found in Li (2023). A calculation step of 10^{-7} m/step is applied to the wall, moving it away from soil masses while recording the normal stress on the interface until it decreases to a stable value. At that case, the soil experiences an active failure, and the resultant normal stress on the interface represents the active earth pressure.

Currently, simulating unsaturated soil behavior with FLAC3D is not common. To address this, a FISH program was developed to calculate apparent cohesion of unsaturated soils based on the unsaturated strength criterion derived in Section 2. The combined cohesion, including both apparent and effective cohesion, is then assigned to the soil behind the wall. Four hypothetical soils, including clay, silt, loess, and sand, are herein included, specific soil and hydraulic parameters summarized in Table 1. The influence of different ratios of width to height on active earth pressure is also discussed. Note that when B/H approaches the infinite, the analytical solution derived by the proposed method is equivalently plane-strain solution. Meanwhile, both completely dray and high infiltration cases are presented as illustrative cases. The water level locates at the slope toe with $z_0 = 0$. Table 3 compares the kinematic approach with numerical calculations, presenting the resultant active earth pressure per unit width. The results show strong agreement with those obtained from the finite difference method (FDM), indicating that the present method is effective for calculating active earth pressure involving in seepage questions. Additionally, an increase in the B/H leads to a higher active earth pressure, suggesting that neglecting the 3D effect would result in a more conservative solution. The plastic shear strain zone from the finite difference model closely matches the kinematic failure surface, as described in Fig. 10, confirming the validity of the proposed method.

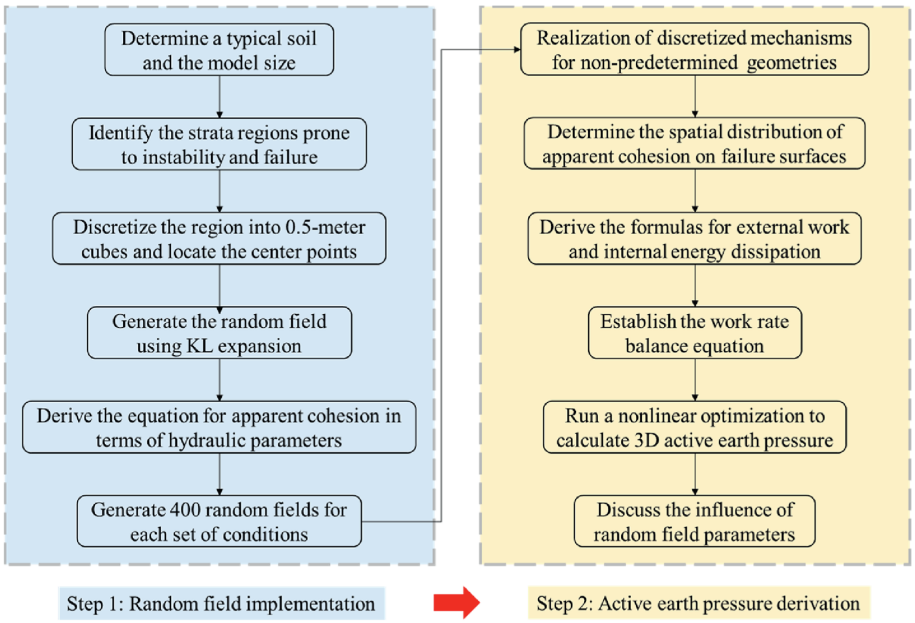

Fig. 8. Derivation process for the active earth pressure considering the spatial variability of permeability.

Table 2
Comparison between the present study and Antão et al. (2016).

B/H	φ (°)	K_a		Relative error
		Antão et al. (2016)	This study	
2	15	0.56	0.549	1.9 %
2	20	0.456	0.449	1.4 %
2	25	0.372	0.364	2.1 %
2	30	0.301	0.293	2.6 %
2	35	0.241	0.229	4.9 %
2	40	0.188	0.181	3.6 %
5	15	0.575	0.573	0.3 %
5	20	0.476	0.474	0.5 %
5	25	0.391	0.387	0.9 %
5	30	0.32	0.319	0.4 %
5	35	0.258	0.247	4.1 %
5	40	0.205	0.201	1.7 %
∞ (2D)	15	0.588	0.588	0.0 %
∞ (2D)	20	0.49	0.489	0.2 %
∞ (2D)	25	0.405	0.404	0.2 %
∞ (2D)	30	0.332	0.332	0.1 %
∞ (2D)	35	0.269	0.259	3.8 %
∞ (2D)	40	0.215	0.216	0.5 %

Note: 2D refers to the case where the model can be regarded as a two-dimensional (2D) plane strain mechanism as the B/H approaches infinity.

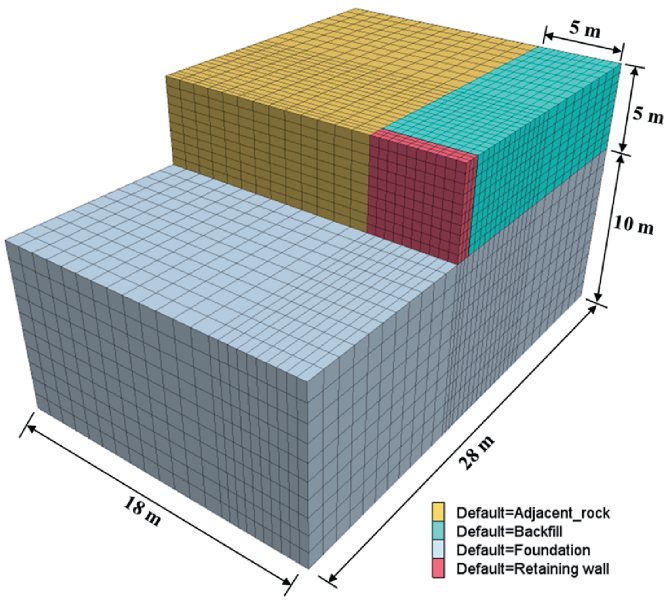

Fig. 9. Numerical modeling and meshing of 3D retaining walls.

4.3. Compared to the random finite difference method

The RFDM is frequently used to address the geotechnical problems by performing an integration of random fields and the FDM. According to Jamshidi Chenari and Alaie (2015), this approach effectively captures the inherent randomness in soil properties, enabling more accurate modeling of soil behaviors. Therefore, the verification was herein carried out by utilizing RFDM. In probability analysis, an appropriate number of MCS is crucial for obtaining converged results. If the number of runs is insufficient, low-probability events may be missed, while an excessively large number of runs can lead to unacceptable computational inefficiency. Thus, optimizing the number of simulations is essential to balance accuracy and efficiency (Zhang et al., 2022).

The size and boundary conditions of the numerical model, with a width-to-height ratio of 2.0, are detailed in Section 4.2. The 3D center point coordinates and boundaries for implementing the saturated hydraulic conductivity random field are derived from the established numerical model. Statistical analyses are performed based on 1000 realizations with $k_s = 5 \times 10^{-7}$ m/s, $COV_{k_s} = 0.3$, $l_x = l_y = 15$ m and $l_z = 1.5$ m. Fig. 11 presents the effect of number of random field realizations on the mean and standard deviation of active earth pressure behind a vertical retaining wall. After around 400 simulations, the mean and standard deviation of active earth pressure stabilize for both RLAM and RFDM. The mean values from RLAM and RFDM differed by less than 10 %, with RLAM exhibiting greater stability and lower variability. RLAM's primary advantage lies in its computational efficiency, delivering results in

Table 3
Comparison between the kinematic approach and numerical calculations.

Soil type	B/H	No seepage			High infiltration		
		This study	FLAC3D	Relative error	This study	FLAC3D	Relative error
Clay	2	72.56	72.70	0.19 %	47.41	49.969	5.12 %
	5	82.08	81.24	1.03 %	59.67	57.98	2.91 %
	∞ (2D)	87.86	86.53	1.54 %	67.25	67.82	0.84 %
Silt	2	69.94	70.19	0.36 %	19.19	19.89	3.52 %
	5	77.59	76.88	0.92 %	31.41	30.74	2.18 %
	∞ (2D)	82.32	81.65	0.82 %	39.06	39.93	2.18 %
Loess	2	73.83	72.51	1.82 %	13.60	14.08	3.41 %
	5	80.13	79.46	0.84 %	24.83	24.17	2.73 %
	∞ (2D)	84.06	83.48	0.69 %	31.83	32.49	2.03 %
Sand	2	73.83	71.34	3.49 %	68.08	68.35	0.40 %
	5	79.52	80.02	0.62 %	73.95	74.73	1.04 %
	∞(2D)	83.10	82.16	1.14 %	77.56	76.88	0.88 %

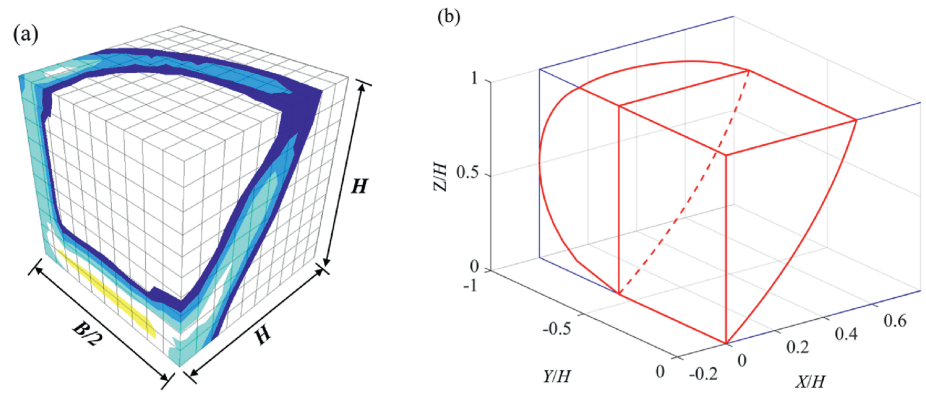

Fig. 10. Comparison with finite difference method: (a) Plastic shear strains calculated by finite difference model, and (b) critical failure surface achieved by the kinematic method.

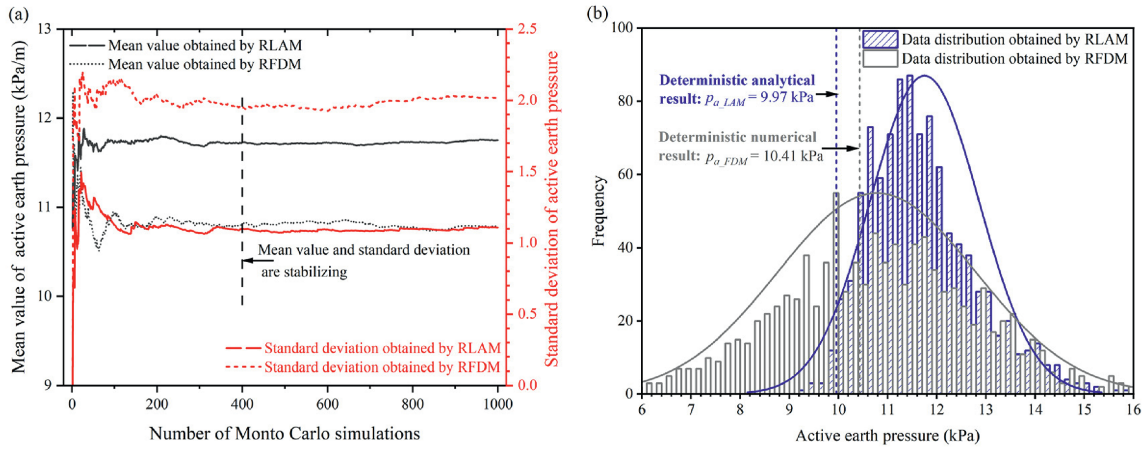

Fig. 11. Influence of RLAM on active earth pressure: (a) The convergence trend of active earth pressure with Monto Carlo simulations, and (b) distribution of active earth pressure.

duration of 12 s compared to 5 min for RFDM. Additionally, RFDM's cost scales steeply with grid size, limiting its use in large or complex simulations. In contrast, RLAM is more efficient and scalable, yielding substantial savings in time and computational resources.

5. Probabilistic analysis

Active earth pressures are highly dependent on equivalent shear strength of unsaturated soils when it involves seepage analysis. Besides, hydraulic properties of soils exhibit notable spatial variations across different layers due to stratification. Therefore, understanding such uncertainty is of much significance to obtain a more accurate solution. A probabilistic analysis is accordingly conducted to assess the influence of parameters associated with the spatial variability on active earth pressures. Unless otherwise specified, the parameters discussed in this section are assumed to maintain their basic values. Section 3.3 establishes an equation for active earth pressures related to soil geometry features, soil parameters, and hydraulic properties. Specially, basic values and ranges of relevant parameters are provided in Table 4. Note that the order of values for c', φ' and k_s in

Table 4
Basic values and ranges of relevant parameters.

Category	Parameter	Symbol	Basic value	Range
Parameters of geometry	Inclined angle	β (°)	90	N/A
	Wall height	H (m)	5	N/A
	Width-to-height ratio	B/H	2	2, 3, 5, 10
Hydraulic and soil properties	Pore size parameter	n	2	2, 3, 4, 5
	Inverse of the air-entry pressure	α (kPa^{-1})	0.005	0.005, 0.01, 0.025, 0.1
	Saturated hydraulic conductivity	k_s (m/s)	5×10^{-8}	5×10^{-8}, 1×10^{-7}, 1×10^{-6}, 3×10^{-5}
	Effective cohesion	c' (kPa)	5	5, 3, 1, 0
	Effective internal frictional angle	φ' (°)	20	20, 25, 28, 30
	Soil weight	γ (kN/m^3)	20	N/A
Parameters related to spatial variability	Normalized horizontal autocorrelation distance	ξ/H	0.5	0.25, 0.5, 1, 2, 4
	Anisotropic ratio	k	0.2	0.1, 0.2, 0.5, 0.8, 1.0
	Coefficient of variation for k_s	COV_{k_s}	0.3	0.1, 0.25, 0.4, 0.55, 0.7

Table 4 aligns with the characteristics of four typical soils, respectively. The normalized horizontal autocorrelation distance ξ/H, anisotropy ratio k and coefficient of variation COV_{k_s} are defined over a specific range.

5.1. Influence of random field parameters

This section aims at investigating the response of four types of unsaturated soils to random field parameters that account for the spatial variability of the saturated hydraulic conductivity. Generally, the autocorrelation distance describes the correlation between random values within a specific range. A larger autocorrelation distance implies smoother variations and greater similarity among adjacent values, while a smaller distance indicates abrupt changes and more pronounced differences. Understanding such autocorrelation distance under different coefficient of variation is essential for grasping the spatial variability of soil properties and its impact on the permeability-related engineering design. The basic values of soil properties for the sensitive analysis can be found in Table 4. As recommended in Section 4.3, approximately 400 simulations can yield a relatively stable active earth pressure. Additionally, to balance computation time and accuracy, the parameters used for the discrete failure mechanism are set to $N_{um} = 200$, and $\delta_\theta = 0.8°$, which can sufficiently obtain a reasonable result. Figs. 12 and 13 present the mean and COV of active earth pressure versus normalized horizontal autocorrelation distance ξ/H and anisotropy ratio k. It is readily found that the spatial variability of soil parameters has a significant impact on mean active earth pressures. Under deterministic conditions, the active earth pressures for the four types of unsaturated soils are 47.41 kPa, 19.19 kPa, 13.60 kPa, 68.08 kPa, respectively. Corresponding deviations from the deterministic analysis are 6.9 %, 17.1 %, 18.3 % and 5.2 %, respectively. The findings suggest that studies neglecting the spatial variability of saturated hydraulic conductivity (Vahedifard et al., 2015; Li, 2023) may yield inaccurate estimates of active earth pressures. An increase in ξ/H exerts minimal influence on the mean active earth pressure. However, the variability of active earth pressure is significantly enhanced, and the magnitude of the covariance increase tends to diminish. These observations align with findings reported in several studies (Cho, 2012; Li et al., 2024). Moreover, such effect is most pronounced for silt, followed by clay, while the effect on loess and sand can be negligible.

Fig. 14 illustrates the influence of COV_{k_s} of saturated hydraulic conductivity k_s on evaluating the active earth pressure. Different soil types exhibit varying responses to COV_{k_s}. Specifically, the mean values for clay and silt significantly increase with the increase in COV_{k_s}. Quantitatively, the active earth pressure generated by clay increases by 48.6 % within the range of COV_{k_s}, followed by silt at 13.2 %, loess at just 1.5 %, while sand shows almost no change. Moreover, the increase in COV_{k_s} inevitably results in greater variability in active earth pressure, a finding that applies to all selected soil types. Among these, silt is the most sensitive to changes in COV_{k_s}, followed by clay, with loess and sandy soil being less affected. However, the magnitude of this increase gradually diminishes. For silt, when COV_{k_s} increases from 0.25 to 0.4, the COV_{k_s} of active earth pressure rises by 26.7 %, while an increase of COV_{k_s} from 0.55 to 0.7 results in only a 9.5 % increase.

5.2. Influence of width-height ratio

To further investigate the impact of geometry size on active earth pressures, four realizations of random fields for clay are generated with $B/H = 2$, 3, 5 and 10. As expected, the increase of ratio B/H impairs the stability of soils. Nevertheless, the growth rate of active earth pressure gradually diminishes as B/H increases. Quantitatively, the mean active earth pressure rises by 12.4 % with B/H ranging from 2 to 3, while this increase drops to 5.5 % as B/H shifts from 5 to 10. When B/H takes a rather large value, 3D effects of soil masses become negligible. This conclusion has also been confirmed in past studies (Antão et al., 2016; Yang and Chen, 2021; Li, 2023). Specifically, under deterministic conditions, the active earth pressures for different B/H were calculated as 47.41, 54.28, 59.67, and 63.69. As illustrated in Figs. 15 and 16, variations in the normalized horizontal autocorrelation distance and anisotropy ratio have minimal impact on mean active earth pressures across different ratios. However, the mean values differ noticeably from those obtained under deterministic conditions. The deviations between the present study and deterministic analysis are 6.93 %, 5.01 %, 3.64 %, and 2.40 %, respectively. Furthermore, increasing B/H encourages reducing the variability of active earth pressure. For instance, for a case of $\xi/H = 0.5$, $k = 0.5$ and $COV_{k_s} = 0.3$, the COV of active earth pressure reduces by 25.8 %, 43.9 %, and 63.5 %, respectively, as B/H increases from 2 to 3, 5, and 10. It indicates that neglecting 3D effects may yield a relatively more conservative solution, though it underestimates fluctuations in active earth pressures.

Fig. 17 illustrates the response of active earth pressure statistics to variations in COV_{k_s} under different B/H values. As depicted in Fig. 17a, the four lines appear nearly parallel. The larger COV_{k_s} can result in a greater mean of active earth pressure. Quantitatively, the mean earth pressure increases by 13.2 %, 10.3 %, 9.9 %, and 9.0 % with COV_{k_s} ranging from 0.1 to 0.7, corresponding to B/H values of 2, 3, 5, and 10, respectively. Furthermore, for different COVs of saturated hydraulic conductivity k_s, it is also found that the COV of active earth pressures gradually increases as B/H decreases, which is similar to the results generated by the normalized horizontal autocorrelation distance and anisotropy ratio.

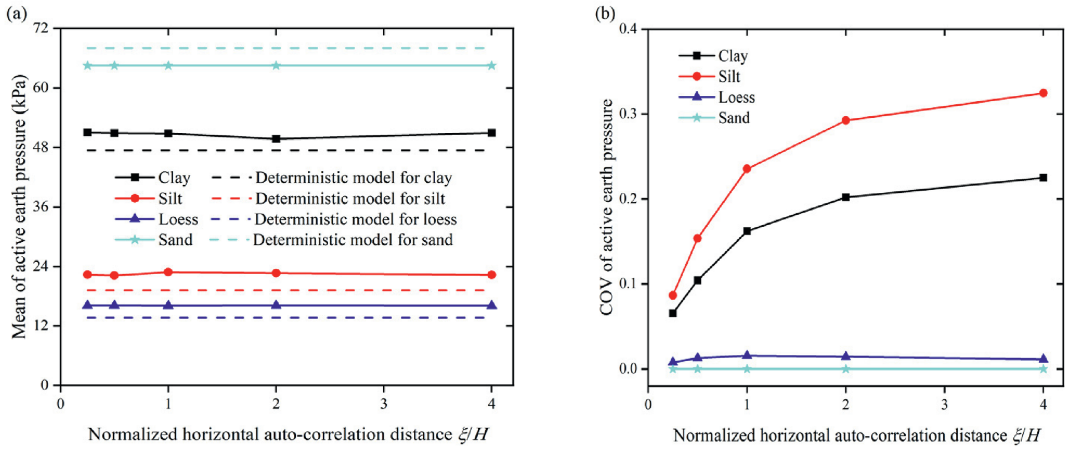

Fig. 12. Influence of normalized autocorrelation distance ξ/H of saturated hydraulic conductivity k_s on statistics of active earth pressure: (a) mean; (b) coefficient of variation COV.

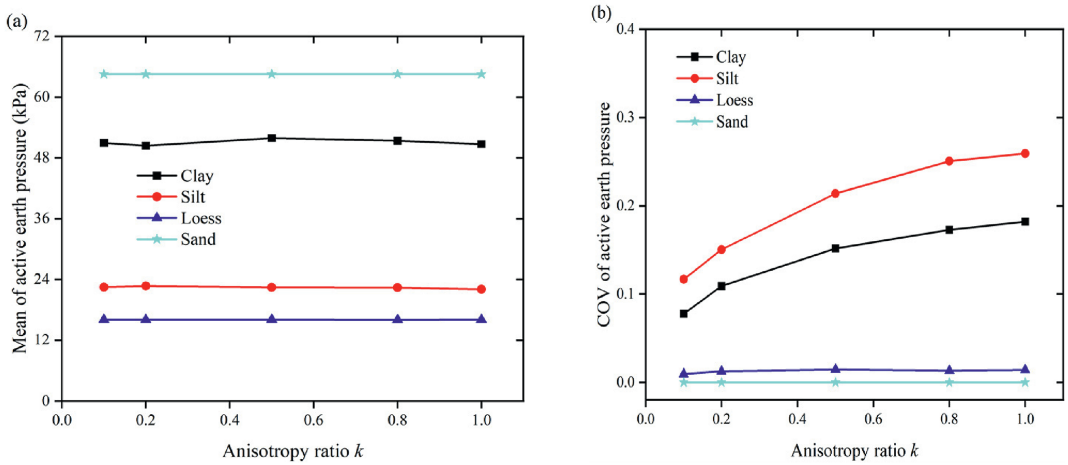

Fig. 13. Influence of anisotropy ratio k of saturated hydraulic conductivity k_s on statistics of active earth pressure: (a) Mean, and (b) coefficient of variation COV.

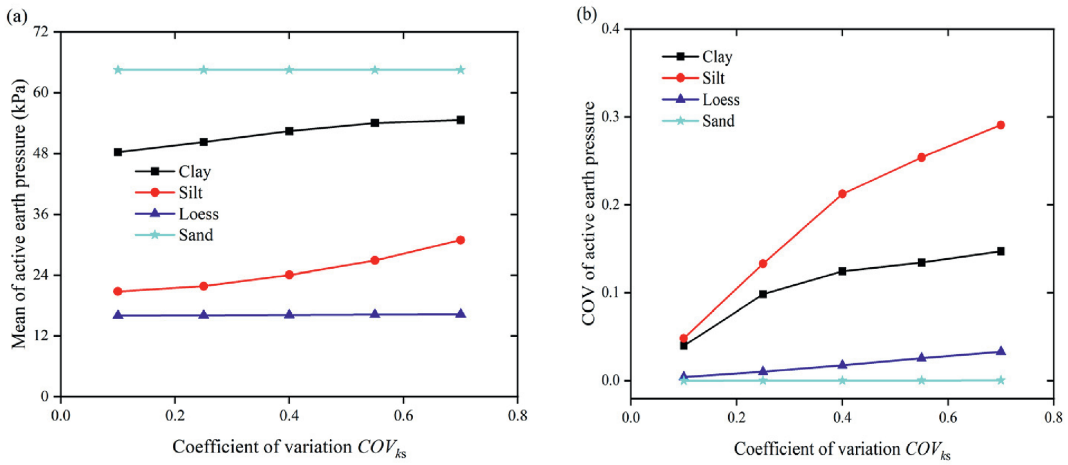

Fig. 14. Influence of coefficient of variation COV_{ks} of saturated hydraulic conductivity k_s on statistics of active earth pressure: (a) Mean, and (b) coefficient of variation COV.

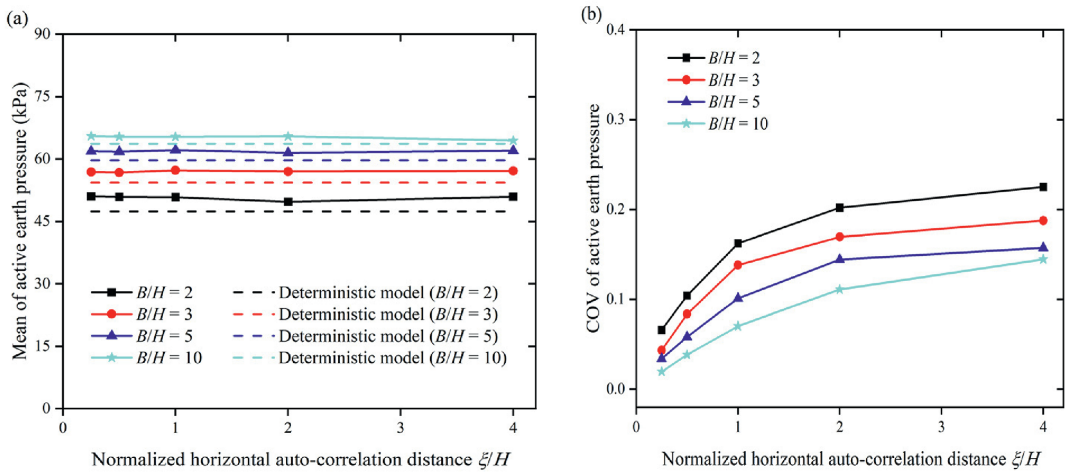

Fig. 15. The response of active earth pressure to width-to-height B/H under different normalized autocorrelation distance ξ/H: (a) Mean, and (b) coefficient of variation COV.

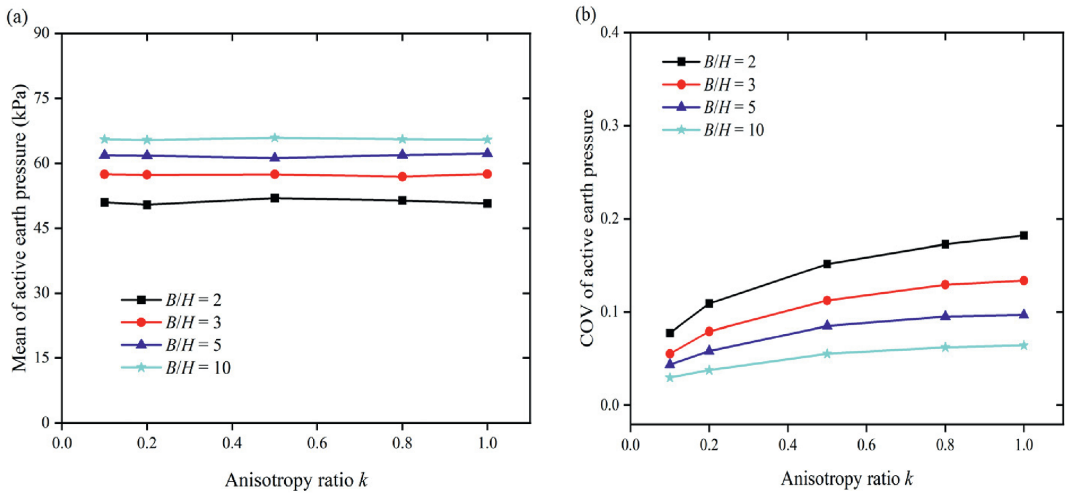

Fig. 16. The response of active earth pressure to width-to-height B/H under different anisotropy ratios k: (a) mean; (b) coefficient of variation COV.

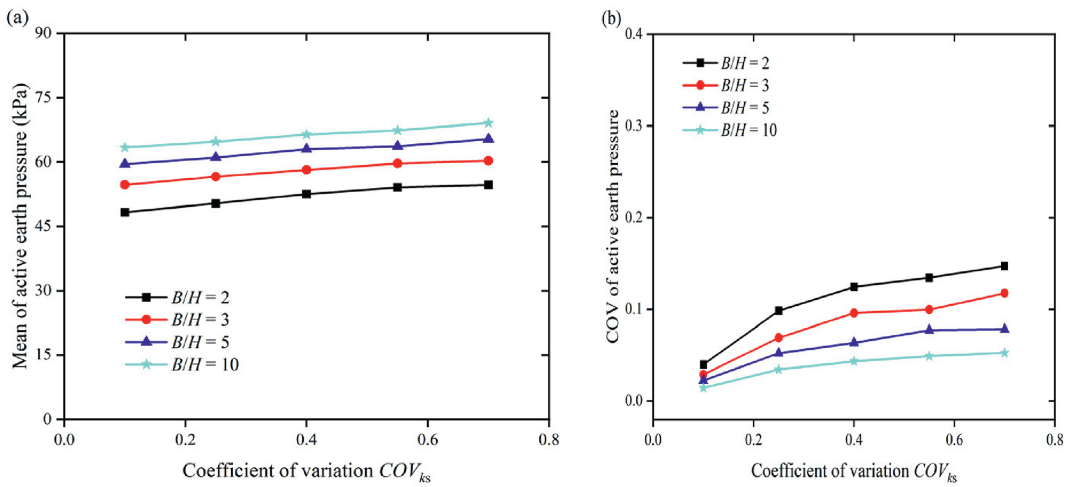

Fig. 17. The response of active earth pressure to width-to-height B/H under different coefficients of variation COV_{k_s}: (a) Mean, and (b) coefficient of variation COV.

6. Reliability-based evaluation for semi-gravity retaining walls

6.1. System failure probability function

The reliability evaluation of retaining wall structures has garnered significant attention. However, current research mainly concentrates on probabilistic analysis involving one or several random variables, remaining confined to a purely mathematical evaluation. These studies usually neglect the impact of spatial variability in hydraulic properties on the reliability evaluation of retaining walls. This section proposes a reliability evaluation method based on extensive uncertainty analyses. A semi-gravity retaining wall is schematically depicted in Fig. 18, with the width of two sides a and b. The backfill is horizontal and level with the retaining wall, with a height of H, and the adhesion between the wall and the foundation is c_2. It is worth mentioning unit width of a wall is taken into consideration in subsequent discussion.

It is well known that the reliability evaluation of wall structures focuses on ensuring stability and safety by addressing potential failure modes: overturning and sliding resistance (Fenton et al., 2005; Gao et al., 2019; Li et al., 2021). The safety factor against overturning instability (FS_1) is defined as the ratio of the resisting moment to the induced moment:

$$FS_1 = \frac{W_1 Mom_{1h} + W_2 Mom_{2h} + P_{av} Mom_{av}}{P_{ah} Mom_{ah}} \tag{29}$$

where W_1 and W_2 are two components of wall weight, with horizontal moment arms: Mom_{1h} and Mom_{2h}, respectively. P_{ah} and P_{av} are horizontal and vertical components of the active earth pressure, with moment arms: Mom_{ah} and Mom_{av}, respectively. According to the geometrical and mechanical relationship, the following expressions can be derived:

$$\begin{cases} W_1 = \frac{1}{2}\gamma_{wall} aH, Mom_{1h} = \frac{2}{3}b + \frac{2}{3}H\cot\beta - \frac{1}{3}a, Mom_{1v} = \frac{2}{3}H \\ W_2 = \frac{1}{2}\gamma_{wall} bH, Mom_{2h} = \frac{2}{3}b + \frac{1}{3}H\cot\beta, Mom_{2v} = \frac{1}{3}H \\ P_{av} = P_a \sin(\delta + \beta - 90^\circ), Mom_{av} = b + \frac{1}{3}H\cot\beta \\ P_{ah} = P_a \cos(\delta + \beta - 90^\circ), Mom_{ah} = \frac{1}{3}H \end{cases} \tag{30}$$

The probability of overturning failure of retaining walls considering spatial variability of saturated hydraulic conductivity, P_{f1}, can be obtained by

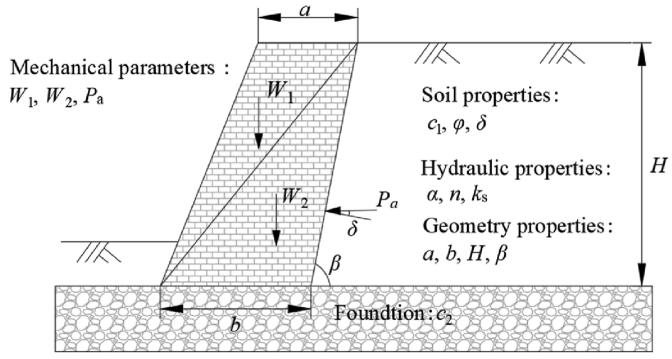

Fig. 18. Longitudinal schematic diagram of a semi-gravity retaining wall.

$$P_{f1} = \frac{1}{N}\sum_{i=1}^{N} I(FS_1) \tag{31}$$

where N denotes the number of MCS required for random field realizations, and I denotes the indicator function, which is defined as: $I(FS_1) = 1$ for $FS_1 < 0$ and $I(FS_1) = 0$ for $FS_1 \geq 0$. The safety factor against the sliding failure of retaining walls (FS_2) is expressed as

$$FS_2 = \frac{bc_2}{P_{ah}} \tag{32}$$

Similarly, the probability of sliding failure, P_{f2}, is written as

$$P_{f2} = \frac{1}{N}\sum_{i=1}^{N} I(FS_2) \tag{33}$$

By combining the sliding and overturning failure modes of the retaining wall, the system failure probability can be defined as

$$P_f = P_{f1} + P_{f2} - P_{f12} \tag{34}$$

where P_{f2} represents the probability of simultaneous overturning and sliding of the retaining wall:

$$P_{f12} = \frac{1}{N}\sum_{i=1}^{N} [I(FS_1) I(FS_2)] \tag{35}$$

6.2. Illustrative example

As elaborated in Section 5.1, autocorrelation distances and COV of saturated hydraulic conductivity exert significant impacts on fluctuations of 3D active earth pressure. Furthermore, it was found that the response of active earth pressure generated by silt to random field parameters is the most sensitive among all types of unsaturated soils. Therefore, this section performs a reliability-based evaluation for a semi-gravity wall resisting silty backfills, with the normalized bottom width of walls as the design index. Other input parameters that do not be emphasized take values from Tables 4 and 5.

Fig. 19 illustrates the responses of system failure probabilities of the semi-gravity retaining wall to the normalized bottom width of walls b/H under three random field parameters: normalized horizontal autocorrelation distance ξ/H, anisotropy ratio k and COV of k_s. As expected, a larger design index, b/H, contributes to a smaller failure probability, P_f. This scenario is always right across all designed cases. As ξ/H increases, the effective range of variation in system failure probabilities gradually widens. Moreover, it is observed that as b/H increases, P_f gradually decreases. The curve exhibits an initial slow decline, followed by a steep descent, gradually leveling off, and ultimately approaching zero. Note that

Table 5
Mean values of input parameters used for the illustrative example.

Input variables	Parameter	Basic value
Inclined angle	β (°)	90
Wall height	H (m)	5
Top width of the wall	a (m)	0.4
Bottom width of the wall	b (m)	0.8
Unit weight of the wall	γ_{wall} (kN/m^3)	24
Adhesion between the wall and foundation	c_2 (kPa)	50
External frictional angle	δ (°)	0
Unit weight of the soil	γ (kN/m^3)	20

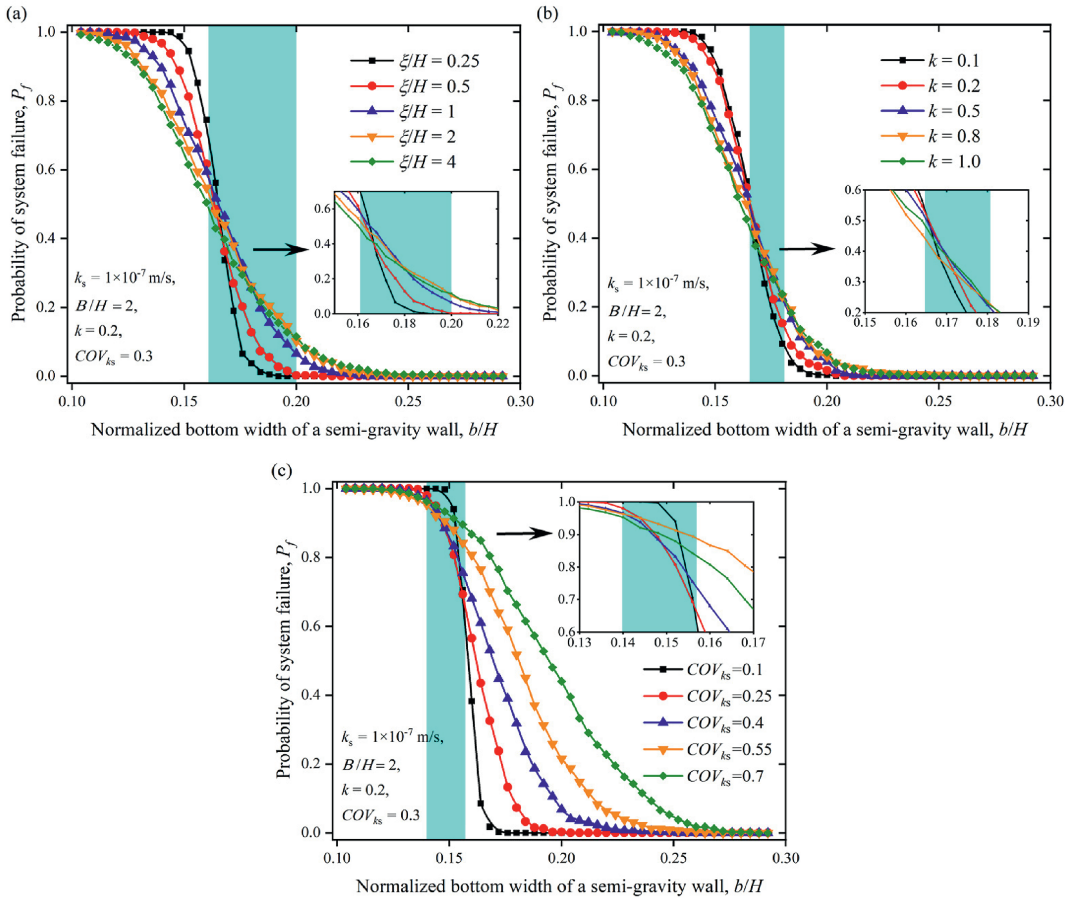

Fig. 19. Influence of random field parameters of saturated hydraulic conductivity on system failure probabilities: (a) Normalized autocorrelation distance ξ/H, (b) anisotropy ratio k; and (c) coefficient of variation COV_{k_s}.

all decreasing curves from Fig. 19a intersect each other within the approximate range from 0.161 to 0.2. Such range is herein defined as the "turning region", as described by the cyan area. It suggests that when ξ/H is smaller than the "turning region", P_f decreases with an increase in ξ/H. While it exceeds the "turning region", P_f increases with an increase in ξ/H. This pattern also applies to the relationship between P_f and k. Additional, Fig. 19c presents the effect of the COV of saturated hydraulic conductivity k_s on P_f. With the increase of COV_{k_s}, the effective variation range of P_f gradually widens. The decay pattern of curves is similar to that in Fig. 19a and b, and for different values of COV_{k_s}, all decay curves intersect approximately within the range of 0.140–0157. Small adjustments in b/H within this range may yield substantial improvements in reliability, potentially reducing construction costs. assuming the design index b/H for $COV_{k_s} = 0.25$ increases from 0.12 to 0.14 as illustrated in Fig. 19c, P_f decreases by 2 %. In contrast, an increase in b/H from 0.14 to 0.16 leads to a 42.3 % reduction in the system failure probability.

The simplicity of 2D reliability evaluation for retaining walls has made it widely popular. However, soil failures often present 3D characterizations in nature. Recent studies have researched the influence of random variables on retaining wall reliability, but the influence of the spatial variability of soil parameters, especially for saturated hydraulic conductivity, remains unaddressed. To further understand the influence of 3D effects on the system failure probability of retaining walls, Fig. 20 exhibits the curves of system failure probabilities versus reliability design index b/H under different width-to-height ratios. It can be observed from Fig. 20, a

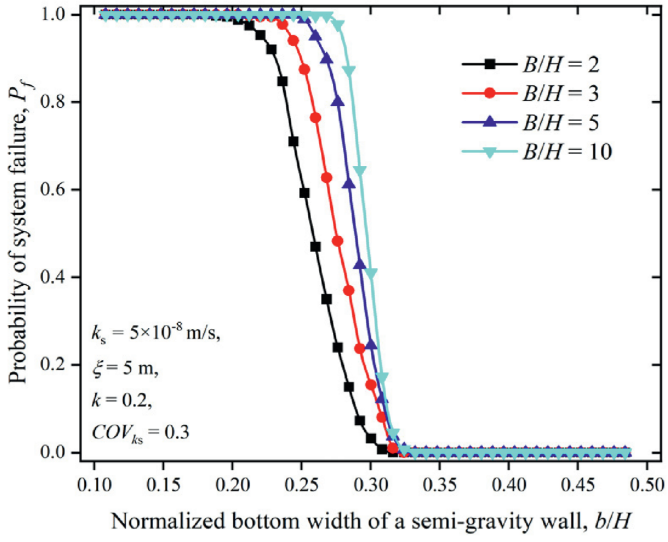

Fig. 20. System failure probabilities for different width-to-height ratios.

larger value of b/H is required to maintain the target reliability at a larger width-to-height ratio B/H. It implies that considering 3D effects may result in an economic saving in terms of the construction of retaining walls. Quantitatively, assuming a system failure probability of 0.2, the required design index b/H for the

retaining wall are 0.279, 0.296, 0.303, and 0.307, respectively. Compared to the conservative design based on plane strain cases, b/H reduced by 3.58 % when $B/H = 3$, while b/H reduced by 9.1 % when $B/H = 2$. It can contribute significantly to achieving an optimal balance between construction cost and performance.

7. Conclusions

The proposed method, by adopting an idealized, non-predefined failure mechanism, can provide a preliminary analytical solution for 3D active earth pressure in complex, nonlinear geological environments. Specifically, the present study discretizes the conventional 3D rotational failure mechanism. An explicit expression of 3D active earth pressures is accordingly derived owing to the energy dissipation principle. Comparisons with the available theoretical method and finite difference method are performed to demonstrate the validation of the present method. The main conclusions can be drawn as follows:

(1) After around 400 simulations, the mean and standard deviation of active earth pressure stabilize for both RLAM and RFDM. The comparison results show high efficiency and accuracy of the proposed method, offering substantial time and computational savings. While the horizontal autocorrelation distance and anisotropic ratio of k_s have little effect on the mean active earth pressure, they significantly increase fluctuations of active earth pressures. This effect is the most obvious for silt, followed by clay, with minimal impact on loess and sand. Moreover, higher COV_{k_s} consistently heightens variability in all soil types.

(2) A reliability-based evaluation method that incorporates the spatial variability of hydraulic properties is developed for semi-gravity retaining walls. As b/H increases, the system failure probability gradually decreases, with curves initially declining slowly, then steepening, and eventually flattening out, approaching zero. Neglecting 3D effects may yield a relatively more conservative solution, though it underestimates fluctuations in active earth pressures. A larger value of b/H is required to maintain the target reliability at a larger width-to-height ratio B/H, suggesting that considering 3D effects may reduce construction costs for retaining walls.

(3) Under different random field design cases, the decay curves of system failure probabilities for a semi-gravity retaining wall always intersect in the "turning region". When b/H is smaller than the region, P_f gradually decreases with the increase of ξ/H, k and COV_{k_s}. While b/H is larger than this region, P_f gradually increases with the increase of ξ/H, k and COV_{k_s}.

Future research will focus on extending the current analytical model to enable its application in the reliability assessment of multilayer soils. Each soil layer will be characterized by its own set of random field parameters to capture the unique hydraulic and mechanical properties inherent in different strata. This extension is expected to enhance the accuracy and applicability of probabilistic analyses in complex, stratified soil environments.

CRediT authorship contribution statement

Hui Chen: Writing – original draft, Methodology, Conceptualization. **Qihao Jiang:** Methodology, Formal analysis. **Dongming Zhang:** Writing – review & editing, Validation, Project administration. **Yadong Xue:** Validation, Investigation. **Hongwei Huang:** Supervision, Investigation.

Declaration of competing interest

The authors declare that they have no known competing financial interests or personal relationships that could have appeared to influence the work reported in this paper.

Acknowledgments

This work was supported by the National Key Research and Development Program of China (Grant No. 2021YFF0502200), and the Shanghai Science and Technology Committee Program (Grant No. 22dz1201202).

References

Antão, A.N., Santana, T.G., Vicente da Silva, M., Guerra, N.M.C., 2016. Three-dimensional active earth pressure coefficients by upper bound numerical limit analysis. Comput. Geotech. 79, 96–104.
Bishop, A.W., 1959. The principle of effective stress. Tek. Ukebl. 106 (39), 859–863.
Castillo, E., Mínguez, R., Ruiz Terán, A., Fernández-Canteli, A., 2004. Design and sensitivity analysis using the probability-safety-factor method. An application to retaining walls. Struct. Saf. 26, 159–179.
Chen, H., Shen, Z., Wang, L., Tian, Y., 2024. Probabilistic undrained bearing capacity of shallow foundations under combined loading in three-dimensional spatially variable soils. Ocean. Eng. 294, 116749.
Cheng, H.Z., Chen, J., Chen, R.P., Chen, G.L., 2019. Reliability study on shield tunnel face using a random limit analysis method in multilayered soils. Tunn. Undergr. Space Technol. 84, 353–363.
Cheng, Z., Zhou, W., Tian, C., 2022. Multi-perspective analysis on rainfall-induced spatial response of soil suction in a vegetated soil. J. Rock Mech. Geotech. Eng. 14 (4), 1280–1291.
Cho, S.E., 2012. Probabilistic analysis of seepage that considers the spatial variability of permeability for an embankment on soil foundation. Eng. Geol. 133–134, 30–39.
Fenton, G.A., Griffiths, D.V., Williams, M.B., 2005. Reliability of traditional retaining wall design. Geotechnique 55 (1), 55–62.
Gao, G.H., Li, D.Q., Cao, Z.J., Wang, Y., Zhang, L., 2019. Full probabilistic design of earth retaining structures using generalized subset simulation. Comput. Geotech. 112, 159–172.
Gardner, W.R., 1958. Some steady-state solutions of the unsaturated moisture flow equation with application to evaporation from a water table. Soil Sci. 85 (4), 228–232.
Griffiths, D.V., Fenton, G.A., 2004. Probabilistic slope stability analysis by finite elements. J. Geotech. Geoenviron. Eng. 130 (5), 507–518.
Gui, S., Zhang, R., Turner, J.P., Xue, X., 2000. Probabilistic slope stability analysis with stochastic hydraulic conductivity. J. Geotech. Geoenviron. Eng. 126 (1), 1–9.
Huder, J., 1972. Stability of bentonite slurry trenches with some experiences in Swiss practice. Fifth ECSMFE 1, 517–522. Madrid.
Huo, M.Z., Chen, W.Z., Wu, G.J., Yuan, J.Q., Li, Y.F., 2023. Probabilistic analysis of tunnel face stability in spatially variable soil. Tunn. Undergr. Space Technol. 141, 105327.
Jamshidi Chenari, R., Alaie, R., 2015. Effects of anisotropy in correlation structure on the stability of an undrained clay slope. Georisk 9 (2), 109–123.
Johari, A., Hajivand, A.K., Binesh, S.M., 2020. System reliability analysis of soil nail wall using random finite element method. Bull. Eng. Geol. Environ. 79, 2777–2798.
Li, T.Z., Gong, W.P., Zhu, C., Tang, H.M., 2024. Stability evaluation of gentle slopes in spatially variable soils using discretized limit analysis method: a probabilistic study. Acta. Geotech. 19, 6319–6335.
Li, Z.W., 2023. Deterministic and Probabilistic Study on three-dimensional Active Earth Pressures Based on Limit Analysis. Central South University, Changsha, China. Ph.D. Thesis.
Li, Z.W., Pan, Q.J., Fei, R.Z., 2021. Probabilistic evaluation of three-dimensional seismic active earth pressures using sparse polynomial chaos expansions. Comput. Geotech. 129, 103869.
Liu, L.L., Cheng, Y.M., Wang, X.M., Zhang, S.H., Wu, Z.H., 2017. System reliability analysis and risk assessment of a layered slope in spatially variable soils considering stratigraphic boundary uncertainty. Comput. Geotech. 89, 213–225.
Liu, W.F., Leung, Y.F., Lo, M.K., 2016. Integrated framework for characterization of spatial variability of geological profiles. Can. Geotech. J. 54, 47–58.
Lu, N., Godt, J.W., Wu, D.T., 2010. A closed-form equation for effective stress in unsaturated soil. Water Resour. Res. 46 (5), W05515.
Lu, N., Likos, W.J., 2004. Unsaturated Soil Mechanics. Wiley & Sons.
Lu, N., Likos, W.J., 2006. Suction stress characteristic curve for unsaturated soil. J. Geotech. Geoenviron. Eng. 132 (2), 131–142.
Masoudian, M.S., Afrapoli, M.A.H., Tasalloti, A., Marshall, A.M., 2019. A general framework for coupled hydro-mechanical modelling of rainfall-induced instability in unsaturated slopes with multivariate random fields. Comput.

Geotech. 115, 103162.
Michalowski, R.L., Drescher, A., 2009. Three-dimensional stability of slopes and excavations. Geotechnique 59 (10), 839–850.
Ng, C.W.W., Qu, C.X., Ni, J.J., Guo, H.W., 2022. Three-dimensional reliability analysis of unsaturated soil slope considering permeability rotated anisotropy random fields. Comput. Geotech. 151, 104944.
Ng, C.W.W., Qu, C.X., Ni, J.J., Guo, H.W., Chen, R., Xue, Q., 2024. Probabilistic analysis of a sustainable landfill cover considering stress-dependent water retention model and copula-based random fields. Eng. Geol. 332, 107460.
Ng, C.W.W., Shi, Q., 1998. A numerical investigation of the stability of unsaturated soil slopes subjected to transient seepage. Comput. Geotech. 22 (1), 1–28.
Pan, Q., Xu, J., Dias, D., 2017. Three-dimensional stability of a slope subjected to seepage forces. Int. J. GeoMech. 17 (8), 04017035.
Piaskowski, A.M., Kowalewski, Z., 1965. Application of thixotrpic clay suspensions for stability of vertical sides of deep trenches without strutting. Proceedings of 6th International Conference on Soil Mechanics and. Foundation Engineering, pp. 526–529.
Pieczyńska-Kozłowska, J., Vessia, G., 2022. Spatially variable soils affecting geotechnical strip foundation design. J. Rock Mech. Geotech. Eng. 14 (3), 886–895.
Qin, C.B., Chian, S.C., 2020. Pseudo-dynamic lateral earth pressures on rigid walls with varying cohesive-frictional backfill. Comput. Geotech. 119, 103289.
Santoso, A.M., Phoon, K.K., Quek, S.T., 2011. Effects of soil spatial variability on rainfall-induced landslides. Comput. Struct. 89 (11–12), 893–900.
Shi, C., Wang, Y., 2023. Stochastic analysis of load-transfer mechanism of energy piles by random finite difference model. J. Rock Mech. Geotech. Eng. 15 (4), 997–1010.
Soubra, A.-H., Galvani, D., Regenass, P., 2000. Three-dimensional active earth pressures. In: European Congress on Computational Methods in Applied Sciences and Engineering (ECCOMAS). Barcelone, Spain, hal-0100904.
Srivastava, A., Babu, G.L.S., Haldar, S., 2010. Influence of spatial variability of permeability property on steady state seepage flow and slope stability analysis. Eng. Geol. 110, 93–101.
Tan, X.H., Dong, X.L., Fei, X.Z., Gong, W.P., Xiu, L.T., Hou, X.L., Ma, H.C., 2020. Reliability analysis method based on KL expansion and its application. Chin. J. Geotech. Eng. 42 (5), 808–816 (in Chinese).
Tsompanakis, Y., Lagaros, N.D., Psarropoulos, P.N., Georgopoulos, E.C., 2009. Probabilistic seismic slope stability assessment of geostructures. Struct. Infrastruct. Eng. 6 (1–2), 179–191.
Vahedifard, F., Leshchinsky Ben, A., Mortezaei, K., Lu, N., 2015. Active earth pressures for unsaturated retaining structures. J. Geotech. Geoenviron. Eng. 141, 04015048.
Vanapalli, S.K., Fredlund, D.G., Pufahl, D.E., Clifton, A.W., 1996. Model for the prediction of shear strength with respect to soil suction. Can. Geotech. J. 33 (3), 379–392.
Yang, X.L., Li, Z.W., 2018. Upper bound analysis of 3D static and seismic active earth pressure. Soil Dynam. Earthq. Eng. 108, 18–28.
Yang, X.L., Chen, H., 2021. Seismic analysis of 3D active earth pressure for unsaturated backfill. Transp. Geotech. 30, 100593.
Zevgolis, I.E., Bourdeau, P.L., 2010. Probabilistic analysis of retaining walls. Comput. Geotech. 37, 359–373.
Zhang, J.Z., Huang, H.W., Zhang, D.M., Zhou, M.L., Tang, C., Liu, D.J., 2021. Effect of ground surface surcharge on deformational performance of tunnel in spatially variable soil. Comput. Geotech. 136, 104229.
Zhang, W., Han, L., Gu, X., Wang, L., Chen, F., Liu, H., 2022. Tunneling and deep excavations in spatially variable soil and rock masses: a short review. Undergr. Space 7, 380–407.
Zhang, Z., Ji, J., Guo, X., Goh, S.H., 2024. Inverse reliability analysis and design for tunnel face stability considering soil spatial variability. J. Rock Mech. Geotech. Eng. 16 (5), 1552–1564.

Mr. Hui Chen is a Ph.D. candidate in Department of Geotechnical Engineering at Tongji University, China. He obtained his bachelor's degree in Collage of Transportation from Wuhan University of Technology, China, his Master's degree in Collage of Civil Engineering from Central South University, China. His research interests include: (1) analytical and numerical methods for soil–tunnel interaction; (2) tunnel risk assessment; and (3) machine learning in geotechnical engineering. He is familiar with MATLAB, FLAC3D and Python. He specializes in lifecycle resilience assessment of tunnel engineering under soil-water coupling uncertainty, focusing on probabilistic modeling of geotechnical variability and multi-hazard performance evaluation.

Dr. Dongming Zhang is a professor at Tongji University, China. He currently serves as the Deputy Director of Department of Geotechnical Engineering at Tongji University, and the Director of the Infrastructure Resilience Research Division at the Shanghai Institute of Disaster Prevention and Relief. His research interest focuses on the evolution and control of tunnel structural safety performance under uncertainty. In this field, he holds several prominent academic positions, including Founding Secretary-General of TC309 (Technical Committee on Machine Learning and Big Data) of the International Society for Soil Mechanics and Geotechnical Engineering (ISSMGE), Secretary-General of the Ministry of Science and Technology Innovation Team on Underground Infrastructure Safety and Risk, Deputy Secretary-General and Chair of the Youth Committee of the Engineering Risk and Insurance Research Branch of the China Civil Engineering Society (CCES), Member of the Council and Deputy Chair of the Youth Committee of the CCES Tunnel and Underground Works Branch.